Nanoscale Advances

ROYAL SOCIETY OF CHEMISTRY

PAPER

View Article Online
View Journal | View Issue

Cite this: *Nanoscale Adv.*, 2022, **4**, 5144

Giant tunneling magnetoresistance in two-dimensional magnetic tunnel junctions based on double transition metal MXene $ScCr_2C_2F_2$†

Zhou Cui,[a] Yinggan Zhang,*[b] Rui Xiong,[a] Cuilian Wen,[a] Jian Zhou,[c] Baisheng Sa*[a] and Zhimei Sun*[c]

Received 14th September 2022
Accepted 22nd October 2022

DOI: 10.1039/d2na00623e

rsc.li/nanoscale-advances

Two-dimensional (2D) transition metal carbides (MXenes) with intrinsic magnetism and half-metallic features show great promising applications for spintronic and magnetic devices, for instance, achieving perfect spin-filtering in van der Waals (vdW) magnetic tunnel junctions (MTJs). Herein, combining density functional theory calculations and nonequilibrium Green's function simulations, we systematically investigated the spin-dependent transport properties of 2D double transition metal MXene $ScCr_2C_2F_2$-based vdW MTJs, where $ScCr_2C_2F_2$ acts as the spin-filter tunnel barriers, 1T-MoS_2 acts as the electrode and 2H-MoS_2 as the tunnel barrier. We found that the spin-up electrons in the parallel configuration state play a decisive role in the transmission behavior. We found that all the constructed MTJs could hold large tunnel magnetoresistance (TMR) ratios over 9×10^5%. Especially, the maximum giant TMR ratio of 6.95×10^6% can be found in the vdW MTJ with trilayer 2H-MoS_2 as the tunnel barrier. These results indicate the potential for spintronic applications of vdW MTJs based on 2D double transition metal MXene $ScCr_2C_2F_2$.

Introduction

A magnetic tunnel junction (MTJ) is an important spintronic device, which consists of two ferromagnets divided by a thin insulating barrier.[1,2] MTJs are widely utilized in magnetic random-access memory, hard disks, and magnetic sensors, *etc.*[3–6] Furthermore, much efforts have been put into the relevant research for MTJs since the tunneling magnetoresistance (TMR) effect was firstly discovered in Fe/Ge/Co multilayer films.[7–9] Herein, the TMR ratio is regarded as one of the most important factors for estimating the performance of MTJs. To enhance the TMR ratio, an effective method involves employing intrinsic magnetic materials with high spin polarizabilities as the electrode material.[10,11] In early years, three-dimensional (3D) magnetic metals such as Fe, Ni, and Co are employed as the ferromagnetic electrodes in MTJs.[12] Unfortunately, the limited spin polarizations lower than 50% result in low TMR ratios for these 3D magnetic metals.[13–15] It is interesting to note that the TMR ratios of MTJs could be improved to a higher level by employing half-metallic (HM) materials as electrodes.[16–18] This is because HM materials possess 100% spin polarization theoretically.[19] However, controlling the quality of the interface between the electrode materials and barrier layers is one of the thorny challenges in 3D HM material-based MTJs.[20] When constructing the MTJs by cleaving 3D materials, the surface dangling bonds will inevitably cause atomic distortion, disorder, and point defects, which could strengthen the interfacial scattering, and lead to the reduction of the TMR ratio.[21]

Recently, the successful synthesis of intrinsic magnetic two-dimensional (2D) materials, such as CrI_3,[22] $Cr_2Ge_2Te_6$,[23] and Fe_3GeTe_2,[24] has opened a new horizon for spintronic devices. Constructing van der Waals (vdW) MTJs *via* perpendicularly stacking magnetic and dielectric 2D materials together through vdW interactions offers impressive performance with high TMR ratios.[25] For example, a TMR ratio of 160% has been experimentally obtained in Fe_3GeTe_2|h-BN|Fe_3GeTe_2 vdW MTJs at low temperatures.[26] Moreover, the TMR ratio of graphene/CrI_3/graphene vdW MTJ up to 19 000% has been experimentally realized by increasing the CrI_3 layer thickness.[27] It is theoretically predicted that a giant zero-bias TMR ratio of up to 48 000% can be achieved using CrOCl/CrOX bilayer as the spin-filter tunnel barriers.[28] On the other hand, the vdW MTJs based on 1T-VSe_2 possess a high TMR ratio of 5600%, and the TMR ratio is sharply increased to 1.7×10^5% by inserting 2H-$MoSe_2$.[29] Two kinds of 6,6,12-graphyne-based molecular magnetic tunnel

[a]*Key Laboratory of Eco-materials Advanced Technology, College of Materials Science and Engineering, Fuzhou University, Fuzhou 350108, P. R. China. E-mail: bssa@fzu.edu.cn*

[b]*College of Materials, Fujian Provincial Key Laboratory of Theoretical and Computational Chemistry, Xiamen University, Xiamen 361005, P. R. China. E-mail: ygzhang@xmu.edu.cn*

[c]*School of Materials Science and Engineering, Center for Integrated Computational Materials Science, International Research Institute for Multidisciplinary Science, Beihang University, Beijing 100191, P. R. China. E-mail: zmsun@buaa.edu.cn*

† Electronic supplementary information (ESI) available. See DOI: https://doi.org/10.1039/d2na00623e

junctions have novel transport behaviors, and the maximum order of magnitude of tunneling magnetoresistance values reaches 10^6%.[30] Wang *et al.* reported the spin-dependent transport properties of a molecular junction made of two manganese phthalocyanine molecules linked by single-walled carbon nanotubes and predicted a high spin-filter efficiency and magnetoresistance ratio.[31] However, it is still challenging to develop 2D materials with intrinsic magnetism to achieve giant TMR ratios in MTJs.

Among various 2D materials, 2D transition metal carbides/nitrides (MXene) materials have attracted much attention due to their fascinating tunable physical and chemical properties from the remarkable variety of chemical diversity.[32–34] MXenes have a general formula of $M_{n+1}X_nT_x$, where M, X, and T represent early transition metals, carbon/nitrogen, and the functional groups (such as O, OH, and F), respectively.[35] It is worth noting that MXene Cr_2C without the surface functional groups is predicted to have intrinsic half-metallicity, and ferromagnetic to antiferromagnetic transitions accompanied by metal-to-insulator transitions can be observed after adsorbing different surface functional groups.[36] Moreover, some intrinsic magnetic MXenes, such as Cr_2NX_2 (X = O, F, OH),[37] Mn_2CT_2 (T = F, Cl, OH, O, and H)[38] are found to possess HM polarization nature and are proposed as potential candidates for vdW MTJs or spin filters.[39,40] Apart from that, double transition metal (DTM) MXenes, including two different transition metals with the general formula of $M_nM'_2X_{n+1}T_x$[41,42] offer more possibilities for fantastic magnetic properties.[43–45] Recently, impressive intrinsic magnetic properties have been found in HM DTM MXenes, such as $ScCr_2C_2F_2$, $ZrCr_2C_2H_2$ and $YCr_2C_2H_2$.[46] Herein, $ScCr_2C_2F_2$ presents a high Curie temperature of 230 K based on the Metropolis Monte Carlo (MC) simulations. Although T_C could be theoretically overestimated, recently good agreement between theoretical results and experimental values have been achieved, for instance, in the case of CrI_3 and Fe_3GeTe_2.[46,47] The MC predicted T_C of 230 K indicates that $ScCr_2C_2F_2$ is anticipated to achieve distinguished MTJ performance as the ferromagnetic electrodes. Therefore, a systematical understanding and optimization of $ScCr_2C_2F_2$-based vdW MTJs are of great interest and importance.

In this work, by employing $ScCr_2C_2F_2$ as the spin-filter tunnel barriers, 1T-MoS_2 and 2H-MoS_2 respectively, as the electrode and tunnel barrier, we have designed and optimized the 1T-MoS_2/$ScCr_2C_2F_2$/2H-MoS_2/$ScCr_2C_2F_2$/1T-MoS_2 vdW MTJs with different stacking configurations and tunnel barrier layer numbers. The interlayer charge transfers, spin-dependent transmission coefficients, spectra projected local density of states, and TMR ratios in the equilibrium state of the constructed vdW MTJs were investigated. The negative binding and formation energies of $ScCr_2C_2F_2$/1T-MoS_2 and $ScCr_2C_2F_2$/2H-MoS_2 heterostructures demonstrate that different layers could stack spontaneously in experiments. Besides, the energetically favorable stacking-II of the $ScCr_2C_2F_2$/1T-MoS_2 interface and stacking-I configurations for the $ScCr_2C_2F_2$/1T-MoS_2 interface are selected to construct the vdW MTJs, which will increase the experimental feasibility. Furthermore, it reveals that the monolayer $ScCr_2C_2F_2$ can maintain half-metallicity with perfect polarization after application in the vdW MTJs. Large TMR ratios of over 9×10^5% are found in all the constructed vdW MTJs, and the maximum TMR ratio of 6.95×10^6% was detected in such vdW MTJ with a trilayer 2H-MoS_2 tunnel barrier. Our findings demonstrate that such DTM MXene-based vdW MTJs have application potential in spintronics.

Computational methods

In order to obtain the interlayer structures before modeling the vdW MTJs, the different stacking configurations for $ScCr_2C_2F_2$/1T-MoS_2 and $ScCr_2C_2F_2$/2H-MoS_2 heterostructures were built using the ALKEMIE platform,[48,49] and investigated based on the density functional theory (DFT) calculations using the Vienna *Ab initio* Simulation Package (VASP).[50] The generalized gradient approximation (GGA) with Perdew–Burke–Ernzerhof (PBE)[51] was used for the exchange and correlation potentials. To better describe the correlation effect of localized 3d electrons in Cr atoms, the GGA + U method with the on-site effective interaction parameter $U = 3.0$ eV was used.[52] The plane-wave cut-off energy of 500 eV and $12 \times 12 \times 1$ K-points were utilized for the optimization and self-consistent calculations. The DFT-D3 method[53,54] was adopted to describe the interlayer van der Waals force. To avoid the interlayer interaction, a 20 Å vacuum was added on top of the 2D materials. The heterostructures were relaxed with the convergence energy for electrons and convergence forces for atoms to 1×10^{-5} eV and 0.01 eV $Å^{-1}$, respectively.

The optimizations and spin-dependent transport calculations of vdW MTJs were implemented using the QuantumWise Atomistix Toolkit (QuantumATK) Q-2021.06 package,[55] based on DFT combined with the nonequilibrium Green's function (NEGF).[56] The generalized gradient approximation (GGA) of the Perdew–Burke–Ernzerhof (PBE)[51] functional with a linear combination of atomic orbitals (LCAO) norm-conserving PseudoDojo pseudopotential[57] were included to deal with the electron exchange and correctional interactions. The double-zeta basis set used to expand wave functions was employed for the calculations.[58] The plane-wave cut-off of 105 Hartree was employed, $10 \times 10 \times 1$ Monkhorst k-point meshes were used for the optimization of the MTJs before performing the spin-dependent transport calculations, and the convergence criterion of the force was set to 0.01 eV $Å^{-1}$. The electron temperature was set at 300 K, which was determined by the Fermi–Dirac distribution *via* the occupation number of each state. When performing the self-consistent calculation, $10 \times 10 \times 1$ Monkhorst k-point meshes were utilized for the central scattering regions. Besides, inspired by the set of electrodes of the recently proposed NiI_2/In_2Se_3 multiferroic devices,[59] the dense enough k-points set was required for the electrodes along the transport direction since they are regarded as the periodic bulk structures for the transport calculations. The Monkhorst k-point meshes for the electrodes were set to $10 \times 10 \times 150$, which is dense enough to ensure the accuracy of the results, and 151×151 Monkhorst–Pack grids were used for the spin-dependent transport calculations.

Results and discussion

In 1T-MoS_2/$ScCr_2C_2F_2$/2H-MoS_2/$ScCr_2C_2F_2$/1T-MoS_2 vdW MTJs, the origin of TMR effects arise from the different densities of states for spin-up and spin-down channels of the $ScCr_2C_2F_2$ layers, which act as the spin-filter tunnel barriers. The corresponding transportation mechanism is illustrated in Fig. 1. When the external magnetic fields are applied in vdW MTJs, the magnetic configurations of the two $ScCr_2C_2F_2$ layers are manipulated to parallel configuration (PC) and antiparallel configuration (APC) states, individually. The tunneling resistances in vdW MTJs vary widely varied in PC and APC. Herein, the TMR ratio is the most important factor in estimating the performance of the magnetic tunnel junctions, which is defined as[60]

$$\mathrm{TMR} = \frac{R_{\mathrm{APC}} - R_{\mathrm{PC}}}{R_{\mathrm{PC}}} = \frac{2P_1P_2}{1 + P_1P_2} \quad (1)$$

where R_{APC} and R_{PC} are the tunneling resistances in PC and APC, respectively. P_1 and P_2 represent the spin polarization of the left and right ferromagnetic materials, respectively. When the device is in the PC state, the spin-up electrons from the left 1T-MoS_2 electrode can hop to the spin-up states around the Fermi level in the left $ScCr_2C_2F_2$ layer, which can further go through the 2H-MoS_2 barrier layer due to the quantum tunneling effect. Subsequently, the spin-up electrons around the Fermi level can hop to the spin-up states of the right $ScCr_2C_2F_2$ layer, and finally hop to the spin-up states of the right 1T-MoS_2 electrode. However, owing to the semiconducting feature of the left $ScCr_2C_2F_2$ in the spin-down channel, a rare state is observed around the Fermi level. Hence, the spin-down electrons from the left 1T-MoS_2 electrode cannot hop to the spin-down states of the left $ScCr_2C_2F_2$ layer. As a result, the vdW MTJ is in a high conductivity state with the contribution of the conductive spin-up electron channel. When the device is in the APC state, both the spin-up and spin-down electrons can hardly pass through the vdW MTJ since the spin-up and spin-down electrons are prevented from hopping to the left and right $ScCr_2C_2F_2$ layers, respectively. As a result, the vdW MTJ is in a high resistance state. Therefore, a considerable difference in the tunneling resistances is obtained from the 1T-MoS_2/$ScCr_2C_2F_2$/2H-MoS_2/$ScCr_2C_2F_2$/1T-MoS_2 vdW MTJ with different spin configurations, where the high conductivity PC state and high resistance APC state are regarded as "1" and "0" states for data storage.[61,62]

The crystal structures of $ScCr_2C_2F_2$, 1T-MoS_2 and 2H-MoS_2 monolayers are shown in Fig. 2a–c. Herein, $ScCr_2C_2F_2$ and 1T-MoS_2 have hexagonal crystal structures with the space group of $P\bar{3}m1$, and 2H-MoS_2 has the space group of $P\bar{6}m2$. The optimized lattice constant of $ScCr_2C_2F_2$ is 3.12 Å. The optimized lattice constants of both 1T-MoS_2 and 2H-MoS_2 are 3.18 Å, which not only agrees well with the experimental values,[63–66] but also exhibits a perfect lattice match with $ScCr_2C_2F_2$. Fig. 2d and f illustrates the calculated band structures for $ScCr_2C_2F_2$, 1T-MoS_2, and 2H-MoS_2 monolayers. From Fig. 2d, $ScCr_2C_2F_2$ shows the metallic properties in the spin-up channel and semiconducting properties in the spin-down channel, revealing its half-metallic magnetic features. On the other hand, from Fig. 2e and f, 1T-MoS_2 and 2H-MoS_2 are demonstrated to be metallic conducting and semiconducting, respectively. Therefore, 1T-MoS_2 and 2H-MoS_2 could be employed as the electrodes and tunnel barrier for the vdW MTJs.

In 1T-MoS_2/$ScCr_2C_2F_2$/2H-MoS_2/$ScCr_2C_2F_2$/1T-MoS_2 vdW MTJs, there are two important vdW interfaces: the $ScCr_2C_2F_2$/1T-MoS_2 interface and the $ScCr_2C_2F_2$/2H-MoS_2 interface. To find the stable interfacial connections in the vdW MTJs, we investigated the different stacking configurations of $ScCr_2C_2F_2$/1T-MoS_2 and $ScCr_2C_2F_2$/2H-MoS_2 heterostructures. As depicted in Fig. 3, each of them owns six different possible stacking configurations. For stacking-I of $ScCr_2C_2F_2$/1T-MoS_2 heterostructure, the Mo atoms of the 1T-MoS_2 layer lie on top of the upper F atoms of the $ScCr_2C_2F_2$ layer, and the upper Cr and C atoms sit right across the upper and bottom S atoms,

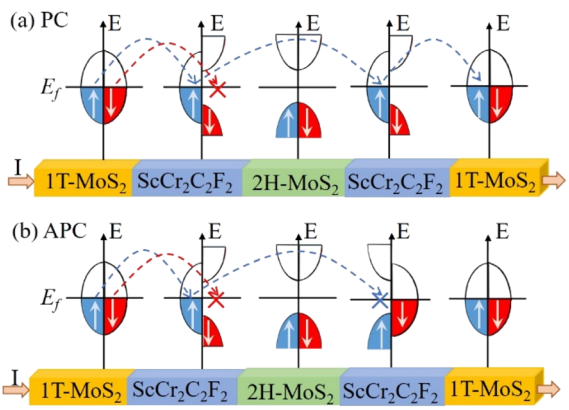

Fig. 1 The electron tunneling mechanism of the 1T-MoS_2/$ScCr_2C_2F_2$/2H-MoS_2/$ScCr_2C_2F_2$/1T-MoS_2 MTJ in (a) PC and (b) APC states.

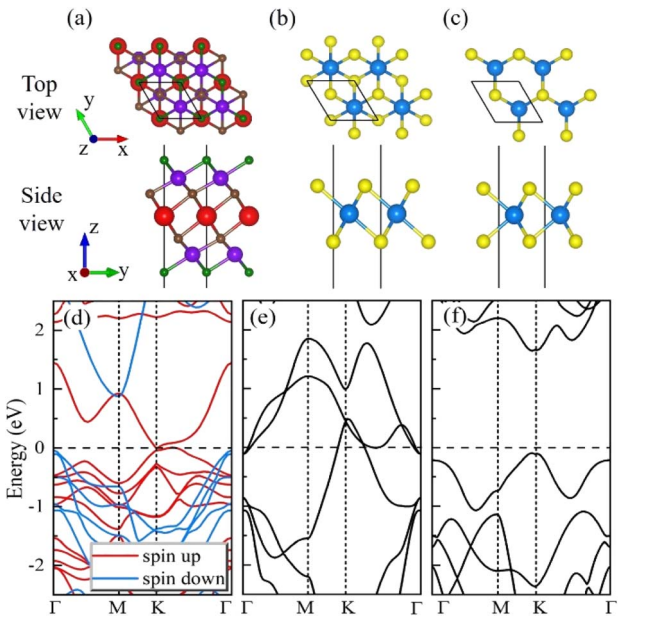

Fig. 2 The crystal structures and band structures for monolayers of (a) and (d) $ScCr_2C_2F_2$, (b) and (e) 1T-MoS_2, (c) and (f) 2H-MoS_2.

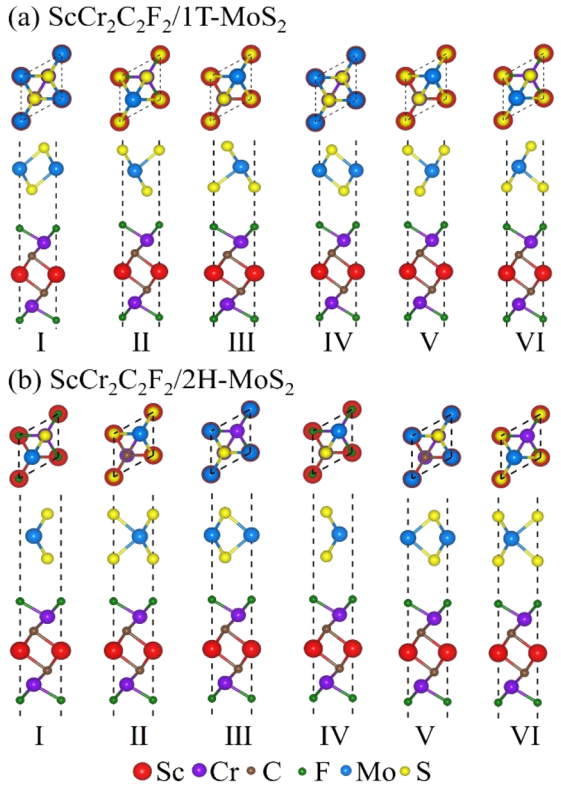

Fig. 3 The structure schematic diagrams of (a) $ScCr_2C_2F_2$/1T-MoS_2 heterostructure and (b) $ScCr_2C_2F_2$/2H-MoS_2 heterostructure with different stacking configurations.

respectively. Stacking-II and stacking-III are obtained from stacking-I by shifting the 1T-MoS_2 layer along the [110] direction of 1/3 and 2/3a, respectively. For stacking-IV, the Mo atoms of the 1T-MoS_2 layer lie on top of the Sc atoms and upper F atoms of the $ScCr_2C_2F_2$ layer, and the upper Cr and C atoms sit right from the bottom and upper S atoms, respectively. Similarly, stacking-V and stacking-VI are obtained from stacking-IV by shifting the 1T-MoS_2 layer along the [110] direction of 1/3 and 2/3a, respectively. For stacking-I of $ScCr_2C_2F_2$/2H-MoS_2 heterostructure, the Mo atoms of the 2H-MoS_2 layer lie on top of the upper C atoms, and the S atoms sit right across the upper Cr atoms. For stacking-IV of $ScCr_2C_2F_2$/2H-MoS_2 heterostructures, the Mo atoms of the 2H-MoS_2 layer lie on top of the upper Cr atoms, and the S atoms sit right across the upper C atoms. The transition of $ScCr_2C_2F_2$/2H-MoS_2 heterostructures from stacking-I to stacking-II/stacking-III and from stacking-IV to stacking-V/stacking-VI is the same as that in the $ScCr_2C_2F_2$/1T-MoS_2 heterostructure.

To estimate the stabilities of the different stacking configurations, the binding energies (E_{bind}) and formation energies (E_{form}) were calculated using the following equations[67,68]

$$E_{bind} = \left(E_{ScCr_2C_2F_2/MoS_2} - E^{fix}_{ScCr_2C_2F_2} - E^{fix}_{MoS_2}\right)/S \quad (2)$$

$$E_{form} = E_{ScCr_2C_2F_2/MoS_2} - E_{ScCr_2C_2F_2} - E_{MoS_2} \quad (3)$$

Table 1 Formation energies E_{form} (meV) and binding energies E_{bind} (meV Å^{-2}) of different stacking configurations of $ScCr_2C_2F_2$/1T-MoS_2 and $ScCr_2C_2F_2$/1T-MoS_2 heterostructures

	$ScCr_2C_2F_2$/1T-MoS_2		$ScCr_2C_2F_2$/2H-MoS_2	
Stacking	E_{form}	E_{bind}	E_{form}	E_{bind}
I	−247.46	−29.88	−208.23	−25.15
II	−255.79	−30.91	−152.59	−18.69
III	−193.68	−23.43	−152.39	−18.65
IV	−250.63	−30.24	−201.82	−24.47
V	−251.70	−30.48	−204.12	−24.64
VI	−193.92	−23.44	−199.54	−24.15

where $E_{ScCr_2C_2F_2/MoS_2}$ is the total energy of the $ScCr_2C_2F_2$/1T-MoS_2 (or $ScCr_2C_2F_2$/2H-MoS_2) heterostructures, $E^{fix}_{ScCr_2C_2F_2}$ and $E^{fix}_{MoS_2}$ stand for the total energies of $ScCr_2C_2F_2$ and 1T-MoS_2 (or 2H-MoS_2) monolayers constrained in the corresponding heterostructure lattice, respectively. S is the interface area. $E_{ScCr_2C_2F_2}$ and E_{MoS_2} represent the free-standing total energies of $ScCr_2C_2F_2$ and 1T-MoS_2 (or 2H-MoS_2) monolayers. The calculated E_{bind} and E_{form} are summarized in Table 1. The negative E_{bind} and E_{form} demonstrate that all the stacking configurations of $ScCr_2C_2F_2$/1T-MoS_2 and $ScCr_2C_2F_2$/2H-MoS_2 heterostructures can form spontaneously. It is worth noting that the stacking-II of $ScCr_2C_2F_2$/1T-MoS_2 heterostructure and stacking-I of $ScCr_2C_2F_2$/1T-MoS_2 heterostructure are more favorable to exist in experiments due to their lowest E_{bind} and E_{form} among various stacking configurations in Table 1. Based on the E_{bind} and E_{form} results, energetically-favorable stacking-II for the $ScCr_2C_2F_2$/1T-MoS_2 interface and stacking-I configurations for the $ScCr_2C_2F_2$/1T-MoS_2 interface were selected to construct the vdW MTJs.

The work function (W_G) and charge transfer between different materials in the MTJ could strongly influence the interfacial effects and the devices' performance.[69,70] To further understand the interfacial effects in the 1T-MoS_2/$ScCr_2C_2F_2$/2H-MoS_2/$ScCr_2C_2F_2$/1T-MoS_2 vdW MTJ, we calculated the electrostatic potential for the 1T-MoS_2, 2H-MoS_2 and $ScCr_2C_2F_2$ monolayers, as shown in Fig. 4a–c, respectively. The work function is defined as the difference between the vacuum energy level and the Fermi level of a 2D material. As depicted in Fig. 4a–c, the values of W_G for 1T-MoS_2, 2H-MoS_2, and $ScCr_2C_2F_2$ monolayers are 5.06, 5.84, and 6.78 eV, respectively. When two different 2D materials are in contact, the electrons of the lower work function side will flow to the higher work function side until their Fermi levels are equal.[71] Therefore, the interlayer charge transfers from 1T-MoS_2/2H-MoS_2 to $ScCr_2C_2F_2$ layers are inferred due to the difference in work functions. To verify the corollary, the charge redistributions in the corresponding 1T-MoS_2/$ScCr_2C_2F_2$/2H-MoS_2/$ScCr_2C_2F_2$/1T-MoS_2 heterostructure are represented from the differential charge density plots in Fig. 4d and e. As seen in the interfacial regions marked with magenta dashed boxes, charge accumulations occur at the F terminations in the $ScCr_2C_2F_2$ layers, and charge depletions are found at the S terminations in the 1T-MoS_2 and 2H-MoS_2 layers.

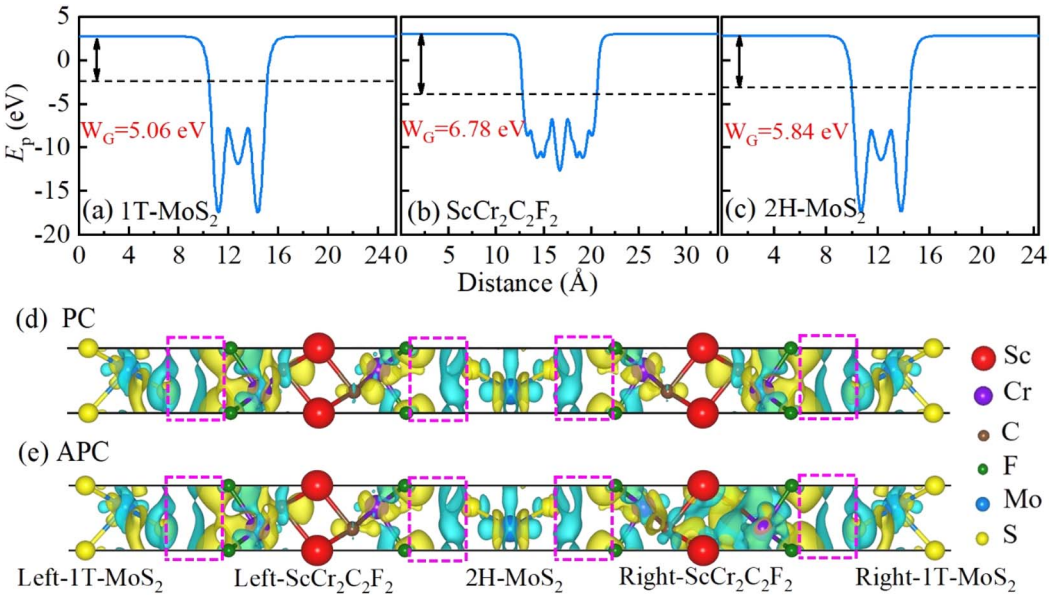

Fig. 4 The electrostatic potential E_p for (a) 1T-MoS_2, (b) monolayer $ScCr_2C_2F_2$ and (c) 2H-MoS_2. The differential charge density of 1T-MoS_2/$ScCr_2C_2F_2$/2H-MoS_2/$ScCr_2C_2F_2$/1T-MoS_2 heterostructure in (d) PC and (e) APC states. The isosurface value is set to 0.0002 e $bohr^{-1,3}$ and the yellow and cyan regions represent the accumulation and depletion of electrons, respectively. The magenta dashed box represents the interfacial region.

To investigate whether the half-metallicity of $ScCr_2C_2F_2$ can be retained in vdW MTJs, we calculated the spin-dependent projected band structures of the 1T-MoS_2/$ScCr_2C_2F_2$/2H-MoS_2/$ScCr_2C_2F_2$/1T-MoS_2 heterostructure when the $ScCr_2C_2F_2$ layers are in PC and APC states. Compared with the band structures of corresponding monolayers in Fig. 2, the projected band structures of the 1T-MoS_2 and 2H-MoS_2 layers move up with respect to the Fermi level, as shown in Fig. 5a, c and e. On the other hand, a conversely downward shift is found for the projected band structures of the $ScCr_2C_2F_2$ layers, as shown in Fig. 5b and d. The energy-level shift agrees well with the charge transfers of electrons in the process of forming the heterostructure we have shown previously. Furthermore, the half-metallic electronic structures of the left and right $ScCr_2C_2F_2$ layers are well maintained, and only the spin-up channel of the PC state is conductive, while the other three channels are insulating. The difference in transmission mainly comes from the spin-up channel of $ScCr_2C_2F_2$ that allows the electrons to pass through, while its spin-down channel prevents electrons from passing through. Therefore, the spin filter effect is mainly contributed by the spin-resolved band structures of $ScCr_2C_2F_2$, rather than the interface between $ScCr_2C_2F_2$ and 2H-MoS_2. Tis phenomenon reveals a large conductivity difference between PC and APC states, which indicates a distinguished performance of the $ScCr_2C_2F_2$-based vdW MTJs.

Furthermore, to understand the thickness effects of the tunnel barrier, odd layer number 2H-MoS_2 with different layer n (n = 1, 3, 5) was taken into account, following the principle of control variables. In the following discussion, 1T-MoS_2/$ScCr_2C_2F_2$/2H-MoS_2/$ScCr_2C_2F_2$/1T-MoS_2 vdW MTJs with one, three and five 2H-MoS_2 layers are abbreviated as MTJ-HM, MTJ-3HM and MTJ-5HM, respectively. The corresponding atomically structured schematics of the vdW MTJs are illustrated in Fig. 6. Herein, after the full-structure optimizations of the vdW MTJs, the relaxed interface distances between different materials are summarized in Table 2. For all the vdW MTJs, the distances between 2H-MoS_2 and $ScCr_2C_2F_2$ (d_{LC} and d_{RC}) are around 2.7–3 Å, and the distances between 1T-MoS_2 and $ScCr_2C_2F_2$ (d_L and d_R) hold smaller values around 2.4–2.5 Å, revealing weak vdW connections in the MTJs.

To investigate the spin-dependent transport properties, we calculated the transmission coefficients at the equilibrium state for the 1T-MoS_2/$ScCr_2C_2F_2$/2H-MoS_2/$ScCr_2C_2F_2$/1T-MoS_2 vdW MTJs. Fig. 7 shows the zero-bias transmission coefficient curves from −1.2 eV to 1.2 eV for MTJ-HM, MTJ-3HM, and MTJ-5HM in PC and APC states. For all the vdW MTJs in the PC state, the maximum spin-up and spin-down transmission coefficients appear around −1 eV below the Fermi level, and the spin-down transmission coefficients suffer more reduction than spin-up transmission coefficients with the energy region approaching the Fermi level. Therefore, the spin-up transmission coefficients at the Fermi level are several orders of magnitude larger than the spin-down transmission coefficients. Herein, the spin-up channel plays a decisive role in the transmission process. When the vdW MTJs are in an APC state, the spin-up transmission coefficients are almost equivalent to the spin-down transmission coefficients of the entire energy region, and the minimum values occur around the Fermi level. Hence, the transmission capacity of both spin channels is tiny in the APC state.

To quantitatively analyse the device performance of the 1T-MoS_2/$ScCr_2C_2F_2$/2H-MoS_2/$ScCr_2C_2F_2$/1T-MoS_2 vdW MTJs,

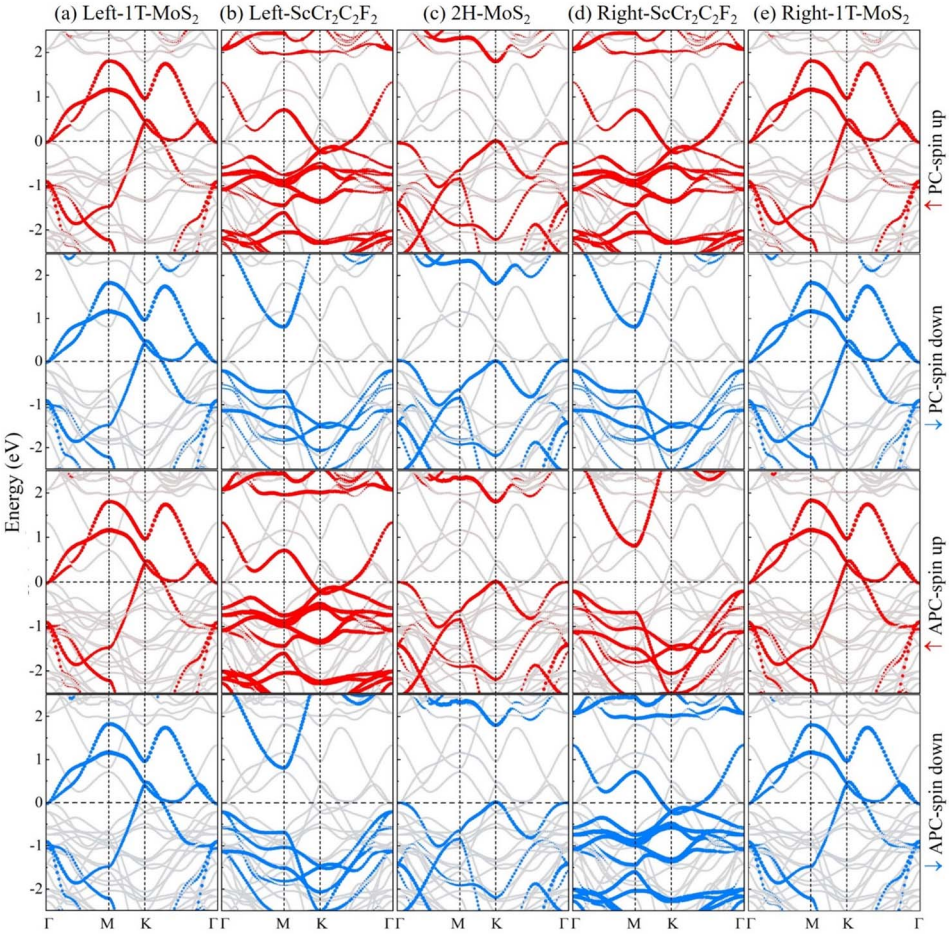

Fig. 5 The spin-dependent projected band structures of (a) left-1T-MoS_2 (b) left-$ScCr_2C_2F_2$ (c) 2H-MoS_2 (d) right-$ScCr_2C_2F_2$ and (e) right-1T-MoS_2 in the 1T-MoS_2/$ScCr_2C_2F_2$/2H-MoS_2/$ScCr_2C_2F_2$/1T-MoS_2 heterostructure.

the TMR ratios can be calculated using the following equation[14,72]

$$\mathrm{TMR} = (G_{\mathrm{PC}} - G_{\mathrm{APC}})/G_{\mathrm{APC}} \times 100\% \quad (4)$$

where G_{PC} and G_{APC} are the total spin-dependent conductance of the PC and APC states, which are defined as

$$G_{\mathrm{PC}} = T^{\uparrow}_{\mathrm{PC}}(E_{\mathrm{f}}) + T^{\downarrow}_{\mathrm{PC}}(E_{\mathrm{f}}) \quad (5)$$

$$G_{\mathrm{APC}} = T^{\uparrow}_{\mathrm{APC}}(E_{\mathrm{f}}) + T^{\downarrow}_{\mathrm{APC}}(E_{\mathrm{f}}) \quad (6)$$

where $T^{\uparrow}_{\mathrm{PC}}(E_{\mathrm{f}})$ and $T^{\downarrow}_{\mathrm{PC}}(E_{\mathrm{f}})$ represent the spin-up and spin-down transmission coefficients at the Fermi level when the vdW MTJs are in the PC state, and $T^{\uparrow}_{\mathrm{APC}}(E_{\mathrm{f}})$ and $T^{\downarrow}_{\mathrm{APC}}(E_{\mathrm{f}})$ represent the spin-up and spin-down transmission coefficients, respectively, at the Fermi level when the vdW MTJs are in the APC state. Table 3 lists the calculated spin-dependent transmission coefficients at the Fermi level, total spin-dependent conductances, and TMR

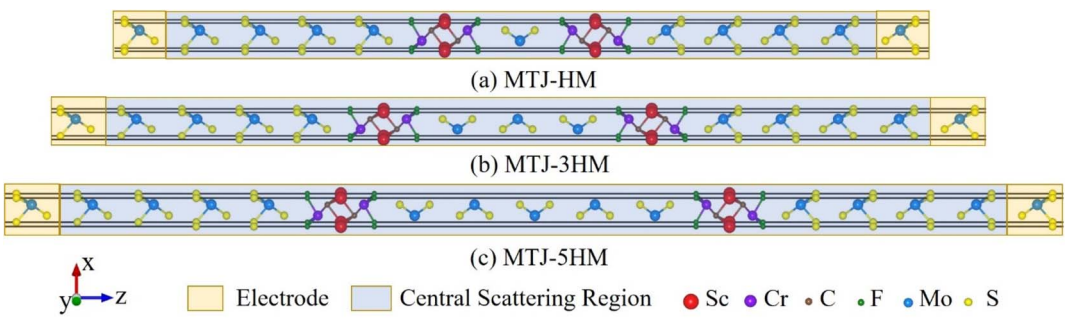

Fig. 6 The schematic illustrations of 1T-MoS_2/$ScCr_2C_2F_2$/2H-MoS_2/$ScCr_2C_2F_2$/1T-MoS_2 vdW MTJs with (a) one (MTJ-HM) (b) three (MTJ-3HM) and (c) five (MTJ-5HM) 2H-MoS_2 tunnel barrier layers.

Table 2 The interface distances d_L, d_{LC}, d_{RC} and d_R (Å) of left-1T-MoS_2/left-$ScCr_2C_2F_2$, left-$ScCr_2C_2F_2$/2H-MoS_2, 2H-MoS_2/right-$ScCr_2C_2F_2$ and right-$ScCr_2C_2F_2$/right-1T-MoS_2 interfaces in different vdW MTJs

MTJs	d_L	d_{LC}	d_{RC}	d_R
MTJ-HM	2.44	3.01	2.93	2.49
MTJ-3HM	2.48	2.76	2.76	2.48
MTJ-5HM	2.48	2.72	2.78	2.44

ratios. It was observed that the total spin-dependent conductances decrease exponentially with the increase in the 2H-MoS_2 barrier layers. It was noted that G_{PC} of MTJ-HM is five orders of magnitude larger than G_{APC}, which results in the giant TMR ratios of 2.95×10^6%. Interestingly, although, G_{PC} and G_{APC} was reduced by several orders of magnitude, when the tunnel-barrier 2H-MoS_2 increases to three layers, the TMR ratio of MTJ-3HM increases to 6.95×10^6% since the corresponding G_{PC} is six orders of magnitude larger than G_{APC}. Besides, when the number of tunnel-barrier 2H-MoS_2 increases to five layers, the TMR ratios of MTJ-5HM decrease to 9.24×10^5%, which is still a considerable giant value. Furthermore, the transmission calculations by including the spin–orbit coupling (SOC) are shown in Table S1.† It is noted that the SOC should contribute to the spin-flip scattering, enhancing the transmission probability in antiparallel configuration and reducing the TMR. Nevertheless, the proposed vdW MTJ devices showed considerable TMR values at a 10^4% level.

Moreover, we calculated the spin-dependent $k_{\|}$-resolved transmission spectrums at the Fermi level to better represent the physical origin of the giant TMR effects in the 1T-MoS_2/$ScCr_2C_2F_2$/2H-MoS_2/$ScCr_2C_2F_2$/1T-MoS_2 vdW MTJs. Herein, Fig. 8 illustrates the transmission spectrum of MTJ-3HM as an example since it shows the highest TMR ratio. For reference, the transmission spectra of MTJ-HM and MTJ-5HM are presented in Fig. S3 and S4,† respectively. Fig. 8a shows that there are six crescent-shaped high transmission regions in the spin-up transmission spectrum for MTJ-3HM in the PC state. However, there is no distinguishable high transmission region in the whole $k_{\|}$-resolved regions for the spin-down transmission spectrum in Fig. 8b. On the other hand, the transmission regions of both spin-up and spin-down channels are similar for MTJ-3HM in the APC state. Herein, it is noted that the transmission capacity of the APC state is several orders of magnitude smaller than that of the PC state, which leads to the apparent TMR effect. In addition, the spin-dependent projected local density of states of MTJ-HM, MTJ-3HM, and MTJ-5HM along the

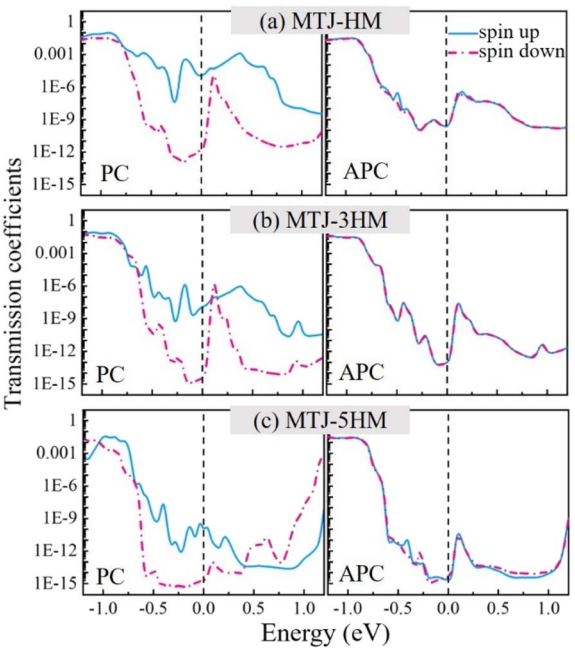

Fig. 7 The transmission coefficients for (a) MTJ-HM, (b) MTJ-3HM, and (c) MTJ-5HM in PC and APC states.

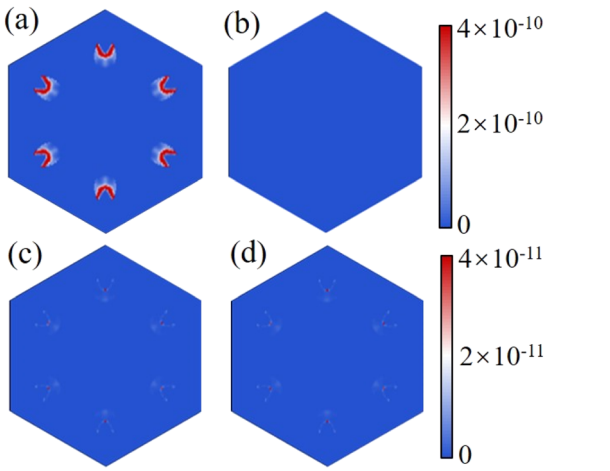

Fig. 8 The spin-dependent $k_{\|}$-resolved transmission spectrums of MTJ-3HM at the Fermi level for (a) spin-up and (b) spin-down channels in the PC state and (c) spin-up and (d) spin-down channels in the APC state.

Table 3 The calculated transmission coefficients (e^2/h) of the spin-up channel in the PC state $T_{PC}^{\uparrow}(E_f)$, spin-down channel in the PC state $T_{PC}^{\downarrow}(E_f)$, spin-up channel in the APC state $T_{APC}^{\uparrow}(E_f)$, and spin-down channel in the APC state $T_{APC}^{\downarrow}(E_f)$, total spin-dependent conductances (e^2/h) in the PC state G_{PC} and the APC state G_{APC}, and TMR ratios for MTJ-HM, MTJ-3HM, and MTJ-5HM devices

MTJs	$T_{PC}^{\uparrow}(E_f)$	$T_{PC}^{\downarrow}(E_f)$	$T_{APC}^{\uparrow}(E_f)$	$T_{APC}^{\downarrow}(E_f)$	G_{PC}	G_{APC}	TMR (%)
MTJ-HM	1.19×10^{-5}	1.76×10^{-12}	2.03×10^{-10}	2.02×10^{-10}	1.19×10^{-5}	4.05×10^{-10}	2.95×10^6
MTJ-3HM	1.30×10^{-8}	3.43×10^{-15}	9.36×10^{-14}	9.27×10^{-14}	1.30×10^{-8}	1.86×10^{-13}	6.95×10^6
MTJ-5HM	5.51×10^{-11}	1.96×10^{-15}	2.32×10^{-15}	3.64×10^{-15}	5.51×10^{-11}	5.96×10^{-15}	9.24×10^5

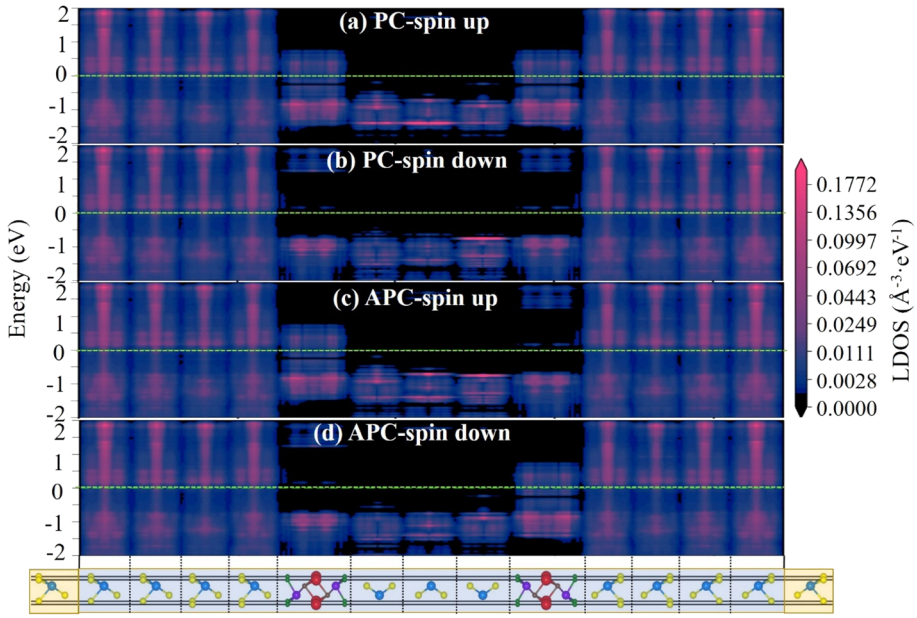

Fig. 9 The spin-dependent projected local density of states of MTJ-3HM for (a) spin-up and (b) spin-down channels in the PC state, (c) spin-up, and (d) spin-down channels in the APC state.

transport direction are shown in Fig. S5, 9 and S6,† respectively. The corresponding vdW MTJ model is illustrated in the bottom panel for reference. Regardless of the PC or APC states, it was observed that the 1T-MoS_2 electrodes and 2H-MoS_2 barriers still exhibit their metallic and semiconducting properties, respectively. However, the $ScCr_2C_2F_2$ monolayer shows metallic properties in the spin-up channel but presents a semiconducting feature in the spin-down channel in the PC state and *vice versa* in the APC state. As a result, in the PC state, for the electron transport process from the left to right in the 1T-MoS_2 electrodes, the spin-up electrons only need to go through the potential barrier of the 2H-MoS_2 layer. However, the spin-down electrons have to overcome a much higher potential barrier, which is from the left and right $ScCr_2C_2F_2$ layers as well as the 2H-MoS_2 layers. On the other hand, in the APC state, the spin-up (spin-down) electrons have to overcome the potential barriers of the right (left) $ScCr_2C_2F_2$ layer and the 2H-MoS_2 layers for the electron transport process from the left to right 1T-MoS_2 electrodes. Therefore, the spin-up electrons in the PC state are proved to play a decisive role in the transmission behavior, which agrees well with our previously electronic structure analysis.

Conclusion

In summary, by combining density functional theory and nonequilibrium Green's function calculations, we investigated the transport properties of 1T-MoS_2/$ScCr_2C_2F_2$/2H-MoS_2/$ScCr_2C_2F_2$/1T-MoS_2 vdW MTJs with different thicknesses of the 2H-MoS_2 tunnel barrier. The different stacking configurations of $ScCr_2C_2F_2$ relative to 1T-MoS_2 and 2H-MoS_2 were firstly studied to determine the stable interface configurations. The calculated formation energies and binding energies indicated that all the interface configurations can form spontaneously. Besides, the interlayer charge transfers from the 1T-MoS_2/2H-MoS_2 to $ScCr_2C_2F_2$ layers can be inferred due to the work function differences. The projected band structures of the corresponding 1T-MoS_2/$ScCr_2C_2F_2$/2H-MoS_2/$ScCr_2C_2F_2$/1T-MoS_2 heterostructure revealed that the $ScCr_2C_2F_2$ monolayer can still maintain half-metallicity with perfect polarization in vdW MTJs. Subsequently, the thickness of the 2H-MoS_2 tunnel barrier was considered for further performance optimizations. It is remarkable to note that all the vdW MTJs hold giant TMR ratios over 9×10^5%, and the maximum TMR ratio of 6.95×10^6% was obtained in vdW MTJ with a trilayer 2H-MoS_2 tunnel barrier, demonstrating the potential of such vdW MTJs for applications.

Conflicts of interest

The authors declare no competing financial interest.

Acknowledgements

This work was supported by the National Natural Science Foundation of China (Grant No. 52201022, 21973012, 51872017, and 51871009), the Natural Science Foundation of Fujian Province (Grant No. 2021J06011, 2020J01351, 2020J01474, and 2021J01590), and the "Qishan Scholar" Scientific Research Project of Fuzhou University.

References

1 J. G. Zhu and C. Park, *Mater. Today*, 2006, **9**, 36–45.
2 A. Hirohata, K. Yamada, Y. Nakatani, I. L. Prejbeanu, B. Diény, P. Pirro and B. Hillebrands, *J. Magn. Magn. Mater.*, 2020, **509**, 166711.

3 A. D. Kent and D. C. Worledge, *Nat. Nanotechnol.*, 2015, **10**, 187–191.
4 J. M. Hu, Z. Li, L. Q. Chen and C. W. Nan, *Nat. Commun.*, 2011, **2**, 553.
5 S. Bhatti, R. Sbiaa, A. Hirohata, H. Ohno, S. Fukami and S. N. Piramanayagam, *Mater. Today*, 2017, **20**, 530–548.
6 A. Hirohata and K. Takanashi, *J. Phys. D: Appl. Phys.*, 2014, **47**, 193001.
7 M. Julliere, *Phys. Lett.*, 1975, **54A**, 225–226.
8 H. Lu, Y. Guo and J. Robertson, *ACS Appl. Mater. Interfaces*, 2021, **13**, 47226–47235.
9 Y. Feng, H. Ding, X. Li, B. Wu and H. Chen, *J. Appl. Phys.*, 2022, **131**, 133901.
10 Y. Guo, Y. Zhang, S. Yuan, B. Wang and J. Wang, *Nanoscale*, 2018, **10**, 18036–18042.
11 Y. Shen, D. Kan, I. C. Lin, M. W. Chu, I. Suzuki and Y. Shimakawa, *Appl. Phys. Lett.*, 2020, **117**, 042408.
12 P. M. Tedrow and R. Meservey, *Phys. Rev. B: Solid State*, 1973, **7**, 318–326.
13 T. Miyazaki and N. Tezuka, *J. Magn. Magn. Mater.*, 1995, **139**, L231–L234.
14 S. Yuasa, T. Nagahama, A. Fukushima, Y. Suzuki and K. Ando, *Nat. Mater.*, 2004, **3**, 868–871.
15 J. S. Moodera, L. R. Kinder, T. M. Wong and R. Meservey, *Phys. Rev. Lett.*, 1995, **74**, 3273–3276.
16 T. Ishikawa, T. Marukame, H. Kijima, K. I. Matsuda, T. Uemura, M. Arita and M. Yamamoto, *Appl. Phys. Lett.*, 2006, **89**, 192505.
17 W. H. Wang, H. Sukegawa, R. Shan, S. Mitani and K. Inomata, *Appl. Phys. Lett.*, 2009, **95**, 182502.
18 B. Yang, L. Tao, L. Jiang, W. Chen, P. Tang, Y. Yan and X. Han, *Phys. Rev. Appl.*, 2018, **9**, 054019.
19 R. A. de Groot, F. M. Mueller, P. G. van Engen and K. H. J. Buschow, *Phys. Rev. Lett.*, 1983, **50**, 2024–2027.
20 T. Scheike, H. Sukegawa, T. Furubayashi, Z. Wen, K. Inomata, T. Ohkubo, K. Hono and S. Mitani, *Appl. Phys. Lett.*, 2014, **105**, 242407.
21 S. Cardoso, P. P. Freitas, C. de Jesus, P. Wei and J. C. Soares, *Appl. Phys. Lett.*, 2000, **76**, 610–612.
22 B. Huang, G. Clark, E. Navarro-Moratalla, D. R. Klein, R. Cheng, K. L. Seyler, D. Zhong, E. Schmidgall, M. A. McGuire, D. H. Cobden, W. Yao, D. Xiao, P. Jarillo-Herrero and X. Xu, *Nature*, 2017, **546**, 270–273.
23 C. Gong, L. Li, Z. Li, H. Ji, A. Stern, Y. Xia, T. Cao, W. Bao, C. Wang, Y. Wang, Z. Q. Qiu, R. J. Cava, S. G. Louie, J. Xia and X. Zhang, *Nature*, 2017, **546**, 265–269.
24 Y. Deng, Y. Yu, Y. Song, J. Zhang, N. Z. Wang, Z. Sun, Y. Yi, Y. Z. Wu, S. Wu, J. Zhu, J. Wang, X. H. Chen and Y. Zhang, *Nature*, 2018, **563**, 94–99.
25 Q. Liu, Y. Wang, Y. Zhao, Y. Guo, X. Jiang and J. Zhao, *Adv. Funct. Mater.*, 2022, 2113126.
26 Z. Wang, D. Sapkota, T. Taniguchi, K. Watanabe, D. Mandrus and A. F. Morpurgo, *Nano Lett.*, 2018, **18**, 4303–4308.
27 T. Song, M. W. Tu, X. Zhang, B. Huang, N. P. Wilson, K. L. Seyler, L. Zhu, T. Taniguchi, K. Watanabe, M. A. McGuire, D. H. Cobden, D. Xiao, W. Yao and X. Xu, *Science*, 2018, **360**, 1214–1218.
28 X. Zhang, Y. Guo, Z. Zhou, X. Zhang, Y. Chen, X. C. Zeng and J. Wang, *Adv. Funct. Mater.*, 2022, 2200154.
29 W. Yang, Y. Cao, J. Han, X. Lin, X. Wang, G. Wei, C. Lv, A. Bournel and W. Zhao, *Nanoscale*, 2021, **13**, 862–868.
30 J. Li, M. Di, Z. Yang, L. C. Xu, Y. Yang and X. Liu, *Phys. Chem. Chem. Phys.*, 2019, **21**, 2734–2742.
31 L. L. Tao and J. Wang, *Nanoscale*, 2017, **9**, 12684–12689.
32 K. Huang, Z. Li, J. Lin, G. Han and P. Huang, *Chem. Soc. Rev.*, 2018, **47**, 5109–5124.
33 K. R. G. Lim, A. D. Handoko, S. K. Nemani, B. Wyatt, H. Y. Jiang, J. Tang, B. Anasori and Z. W. Seh, *ACS Nano*, 2020, **14**, 10834–10864.
34 F. Shahzad, A. Iqbal, H. Kim and C. M. Koo, *Adv. Mater.*, 2020, **32**, 2002159.
35 M. Alhabeb, K. Maleski, B. Anasori, P. Lelyukh, L. Clark, S. Sin and Y. Gogotsi, *Chem. Mater.*, 2017, **29**, 7633–7644.
36 C. Si, J. Zhou and Z. Sun, *ACS Appl. Mater. Interfaces*, 2015, **7**, 17510–17515.
37 Q. Sun, J. Li, Y. Li, Z. Yang and R. Wu, *Appl. Phys. Lett.*, 2021, **119**, 062404.
38 J. He, P. Lyu and P. Nachtigall, *J. Mater. Chem. C*, 2016, **4**, 11143–11149.
39 E. Balci, U. O. Akkus and S. Berber, *ACS Appl. Mater. Interfaces*, 2019, **11**, 3609–3616.
40 J. Yang, S. Zhang, L. Li, A. Wang, Z. Zhong and L. Chen, *Matter*, 2019, **1**, 1304–1315.
41 B. Anasori, Y. Xie, M. Beidaghi, J. Lu, B. C. Hosler, L. Hultman, P. R. C. Kent, Y. Gogotsi and M. W. Barsoum, *ACS Nano*, 2015, **9**, 9507–9516.
42 W. Hong, B. C. Wyatt, S. K. Nemani and B. Anasori, *MRS Bull.*, 2020, **45**, 850–861.
43 Y. W. Cheng, J. H. Dai, Y. M. Zhang and Y. Song, *J. Phys. Chem. C*, 2018, **122**, 28113–28122.
44 L. Dong, H. Kumar, B. Anasori, Y. Gogotsi and V. B. Shenoy, *J. Phys. Chem. Lett.*, 2017, **8**, 422–428.
45 Z. Jing, H. Wang, X. Feng, B. Xiao, Y. Ding, K. Wu and Y. Cheng, *J. Phys. Chem. Lett.*, 2019, **10**, 5721–5728.
46 Y. Zhang, Z. Cui, B. Sa, N. Miao, J. Zhou and Z. Sun, *Nanoscale Horiz.*, 2022, **7**, 276–287.
47 Z. Shen, X. Bo, K. Cao, X. Wan and L. He, *Phys. Rev. B*, 2021, **103**, 085102.
48 G. Wang, L. Peng, K. Li, L. Zhu, J. Zhou, N. Miao and Z. Sun, *Comput. Mater. Sci.*, 2021, **186**, 110064.
49 G. Wang, K. Li, L. Peng, Y. Zhang, J. Zhou and Z. Sun, *Acta Metall. Sin.*, 2022, **58**, 75–88.
50 G. Kresse and J. Furthmüller, *Phys. Rev. B: Condens. Matter Mater. Phys.*, 1996, **54**, 11169.
51 J. P. Perdew, K. Burke and M. Ernzerhof, *Phys. Rev. Lett.*, 1996, **77**, 3865.
52 H. Kumar, N. C. Frey, L. Dong, B. Anasori, Y. Gogotsi and V. B. Shenoy, *ACS Nano*, 2017, **11**, 7648–7655.
53 S. Grimme, J. Antony, S. Ehrlich and H. Krieg, *J. Chem. Phys.*, 2010, **132**, 154104.
54 S. Grimme, S. Ehrlich and L. Goerigk, *J. Comput. Chem.*, 2011, **32**, 1456–1465.

55 S. Smidstrup, T. Markussen, P. Vancraeyveld, J. Wellendorff, J. Schneider, T. Gunst, B. Verstichel, D. Stradi, P. A. Khomyakov, U. G. Vej-Hansen, M. E. Lee, S. T. Chill, F. Rasmussen, G. Penazzi, F. Corsetti, A. Ojanpera, K. Jensen, M. L. N. Palsgaard, U. Martinez, A. Blom, M. Brandbyge and K. Stokbro, *J. Phys.: Condens. Matter*, 2020, **32**, 015901.

56 M. Brandbyge, J. L. Mozos, P. Ordejón, J. Taylor and K. Stokbro, *Phys. Rev. B: Condens. Matter Mater. Phys.*, 2002, **65**, 165401.

57 M. J. van Setten, M. Giantomassi, E. Bousquet, M. J. Verstraete, D. R. Hamann, X. Gonze and G. M. Rignanese, *Comput. Phys. Commun.*, 2018, **226**, 39–54.

58 V. Blum, R. Gehrke, F. Hanke, P. Havu, V. Havu, X. Ren, K. Reuter and M. Scheffler, *Comput. Phys. Commun.*, 2009, **180**, 2175–2196.

59 Y. Guo, X. Yu, Y. Zhang, X. Zhang, S. Yuan, Y. Li, S. A. Yang and J. Wang, *ACS Nano*, 2022, **16**, 11174–11181.

60 M. Julliere, *Phys. Lett.*, 1975, **54A**, 225–227.

61 Z. Diao, Z. Li, S. Wang, Y. Ding, A. Panchula, E. Chen, L. C. Wang and Y. Huai, *J. Phys.: Condens. Matter*, 2007, **19**, 165209.

62 J. Z. Sun and D. C. Ralph, *J. Magn. Magn. Mater.*, 2008, **320**, 1227–1237.

63 M. Kan, J. Y. Wang, X. W. Li, S. H. Zhang, Y. W. Li, Y. Kawazoe, Q. Sun and P. Jena, *J. Phys. Chem. C*, 2014, **118**, 1515–1522.

64 R. Kappera, D. Voiry, S. E. Yalcin, B. Branch, G. Gupta, A. D. Mohite and M. Chhowalla, *Nat. Mater.*, 2014, **13**, 1128–1134.

65 F. Raffone, C. Ataca, J. C. Grossman and G. Cicero, *J. Phys. Chem. Lett.*, 2016, **7**, 2304–2309.

66 J. N. Coleman, M. Lotya, A. O'Neill, S. D. Bergin, P. J. King, U. Khan, K. Young, A. Gaucher, S. De, R. J. Smith, I. V. Shvets, S. K. Arora, G. Stanton, H. Y. Kim, K. Lee, G. T. Kim, G. S. Duesberg, T. Hallam, J. J. Boland, J. J. Wang, J. F. Donegan, J. C. Grunlan, G. Moriarty, A. Shmeliov, R. J. Nicholls, J. M. Perkins, E. M. Grieveson, K. Theuwissen, D. W. McComb, P. D. Nellist and V. Nicolosi, *Science*, 2011, **331**, 568.

67 J. Liao, B. Sa, J. Zhou, R. Ahuja and Z. Sun, *J. Phys. Chem. C*, 2014, **118**, 17594–17599.

68 L. F. Wang, T. B. Ma, Y. Z. Hu, Q. Zheng, H. Wang and J. Luo, *Nanotechnology*, 2014, **25**, 385701.

69 S. Gbadamasi, M. Mohiuddin, V. Krishnamurthi, R. Verma, M. W. Khan, S. Pathak, K. Kalantar-Zadeh and N. Mahmood, *Chem. Soc. Rev.*, 2021, **50**, 4684–4729.

70 X. Hu, X. Li, G. Li, T. Ji, F. Ai, J. Wu, E. Ha and J. Hu, *Adv. Funct. Mater.*, 2021, **31**, 2011284.

71 J. Kang, W. Liu, D. Sarkar, D. Jena and K. Banerjee, *Phys. Rev. X*, 2014, **4**, 031005.

72 S. S. Parkin, C. Kaiser, A. Panchula, P. M. Rice, B. Hughes, M. Samant and S. H. Yang, *Nat. Mater.*, 2004, **3**, 862–867.